Shell-model half-lives including first-forbidden contributions for *r*-process waiting-point nuclei

Q. Zhi,[1,2,3] E. Caurier,[4] J. J. Cuenca-García,[2] K. Langanke,[1,2,5] G. Martínez-Pinedo,[1,2] and K. Sieja[4]

[1]*Institut für Kernphysik (Theoriezentrum), Technische Universität Darmstadt, Schlossgartenstraße 2, 64289 Darmstadt, Germany*

[2]*GSI Helmholtzzentrum für Schwerioneneforschung, Planckstraße 1, 64291 Darmstadt, Germany*

[3]*School of Physics and Electronic Science, Guizhou Normal University, 550001 Guiyang, People's Republic of China*

[4]*Université de Strasbourg, IPHC, 23 rue du Loess, CNRS, UMR7178, 67037 Strasbourg, France*

[5]*Frankfurt Institute of Advanced Studies, Ruth-Moufang Straße 1, 60438 Frankfurt, Germany*

(Received 1 December 2012; published 15 February 2013)

We have performed large-scale shell-model calculations of the half-lives and neutron-branching probabilities of the *r*-process waiting-point nuclei at the magic neutron numbers $N = 50$, 82, and 126. The calculations include contributions from allowed Gamow-Teller and first-forbidden transitions. We find good agreement with the measured half-lives for the $N = 50$ nuclei with charge numbers $Z = 28$–32 and for the $N = 82$ nuclei ^{129}Ag and ^{130}Cd. The contribution of forbidden transitions reduce the half-lives of the $N = 126$ waiting-point nuclei significantly, while they have only a small effect on the half-lives of the $N = 50$ and 82 *r*-process nuclei.

DOI: 10.1103/PhysRevC.87.025803 PACS number(s): 21.60.Cs, 21.10.Tg, 23.40.−s, 26.30.Hj

I. INTRODUCTION

Although the actual site of the astrophysical *r*-process is still not known with certainty, it is commonly accepted that it occurs in an explosive environment of relatively high temperatures ($T \approx 10^9$ K) and very high neutron densities ($>10^{20}$ cm^{-3}) [1–5]. Under such conditions, neutron captures are much faster than competing β decays and the *r*-process path in the nuclear chart proceeds through a chain of extremely neutron-rich nuclei with relatively low and approximately constant neutron separation energies ($S_n \lesssim 3$ MeV). Due to the relatively stronger binding of nuclei with magic neutron numbers, the neutron separation energies show discontinuities at the magic numbers $N = 50$, 82, and 126. As a consequence, the *r*-process matter flow slows down when it reaches these magic neutron nuclei and has to wait for several β decays (which are also longer than for other nuclei on the *r*-process path) to occur before further neutron captures are possible, carrying the mass flow to heavier nuclei. Thus matter is accumulated at these *r*-process waiting points associated with the neutron numbers $N = 50$, 82, and 126, leading to the well-known peaks in the observed *r*-process abundance distribution.

The β half-lives of the waiting points have at least two important effects on the *r*-process dynamics and abundance distributions. First, they mainly determine the time it takes the mass flow within the *r*-process to transmute seed nuclei to heavy nuclei in the third peak around $A \sim 200$. Second, in the astrophysical environment the nuclear *r*-process time scale (given by the sum of β half-lives of nuclei in the *r*-process path) competes with some dynamical time scale of the environment, e.g., the expansion time scale of the ejected matter. If the *r*-process path and half-lives were known, the reproduction of the abundance distribution can be used to constrain the conditions of the astrophysical environment. If the *r*-process has sufficient time for β-flow equilibrium to establish, the relative elemental abundances are proportional to the β half-life [6].

Despite their importance, only a few half-lives of waiting points with magic neutron numbers $N = 50$ and 82 are known experimentally [7–10], and no experimental data exist yet for the $N = 126$ waiting points. The situation is expected to improve in the near future with the advent of new experimental facilities. For example, the β-decay half-lives of 38 new neutron-rich isotopes from Kr to Tc close to the *r*-process path have been measured at the new Radioactive Ion Beam Factory facility at RIKEN [11]. Furthermore, researchers at GSI have measured half-lives of nuclei close to $N = 126$ using a novel analysis method [12]. Despite this progress, the half-lives needed for *r*-process simulations have mainly relied on theoretical estimates. As the Q values involved are rather low, such calculations have traditionally been based on allowed (i.e., Gamow-Teller, GT) transitions. Most of these studies used the quasiparticle random phase approximation (QRPA) either on top of semiempirical global models [13–15] or the Hartree-Fock-Bogoliubov method [16]. Although the calculations give a fair account of the few experimental half-lives, it is well known that these models underestimate the correlations among nucleons which pull down the GT strength to low energies. This shortcoming is overcome within the interacting shell model, which indeed describes the measured half-lives of *r*-process waiting-point nuclei very well [17–19].

It is expected that the appearance of intruder single-particle states with different parity may have influence on the low-energy spectra of the *r*-process waiting-point nuclei. Thus it is conceivable that first-forbidden transitions might contribute to the half-lives of these nuclei. A first attempt to estimate such forbidden contributions has been taken within the gross theory [14]. This model, however, has been found to be rather inaccurate when applied to Gamow-Teller transitions. More recently, Borzov extended the QRPA studies based on the Fayans energy functional to a consistent treatment of allowed and first-forbidden contributions to *r*-process half-lives [20]. While these calculations find that forbidden contributions give only a small correction to the half-lives of the $N = 50$ and $N = 82$ waiting-point nuclei, they result in a significant reduction of the $N = 126$ half-lives. This important finding has been our motivation to extend our shell-model calculations of waiting-point half-lives to include also first-forbidden transitions. We

expect that not only will correlations among nucleons affect the half-lives, but reliable descriptions of the detailed allowed and forbidden strength functions are needed to estimate the probabilities for β-delayed neutron-emission rates, which are known to be important for describing the decay of the r-process nuclei toward stability after freeze-out.

We note that GT and higher multipole transitions are relevant to describe neutrino-nucleus reactions, which are important in many astrophysical sites [18,21]. Traditionally, these reactions have been studied within the random phase approximation [22,23], including nuclei relevant to r-process nucleosynthesis [24–26]. In an interesting recent development, neutrino-induced reactions on light nuclei with relevance to neutrino nucleosynthesis [27,28] have been calculated on the basis of the shell model, including GT and first-forbidden transitions [29,30].

II. SHELL MODEL AND β-DECAY THEORY

In our half-life calculations, we consider allowed and first-forbidden contributions. These are obtained using the diagonalization shell mode code NATHAN developed by Caurier [31,32] to calculate the initial and final nuclear states and the corresponding nuclear transition matrix elements. Model spaces and residual interactions are discussed for the three different sets of waiting-point nuclei with $N = 50$, 82, and 126 individually. The partial half-life, t, for a transition between an initial (normally the ground state) and a final nuclear state is related to the phase-space factor by

$$ft = K = 6146 \text{ s}. \tag{1}$$

The phase factor has the form

$$f = \int_1^{W_0} C(W)F(Z,W)(W^2-1)^{1/2}W(W_0-W)^2 dW\,. \tag{2}$$

$C(W)$ is the so-called shape factor that depends on the electron energy, and W is in units of electron mass. W_0 is the maximum electron energy, also in electron mass units, that is given by the difference in nuclear masses between the initial and final nuclear states, $W_0 = Q/(m_e c^2) = (M_i - M_f)/m_e$. $F(Z,W)$ is the Fermi function that corrects the phase space integral for the Coulomb distortion of the electron wave function near the nucleus. The partial decay rate is related to the partial half-life: $\lambda = \ln 2/t$. The total decay rate is given by summing over the partial decay rates to all possible final states.

For allowed transitions, the shape factor does not depend on the electron energy and for β^- decay has the form

$$C(W) = B(GT). \tag{3}$$

The GT reduced transition probability is given by

$$B(GT) = \left(\frac{g_A}{g_V}\right)^2 \frac{\langle f|\left|\sum_k \boldsymbol{\sigma}^k \boldsymbol{t}_-^k\right||i\rangle^2}{2J_i+1}, \tag{4}$$

where the matrix element is reduced with respect to the spin operator $\boldsymbol{\sigma}$ only (Racah convention [33]) and the sum runs over all nucleons. For the isospin-lowering operator, we use the convention $\boldsymbol{t}_- n = p$. Finally, $(g_A/g_V) = -1.2701(25)$ is the ratio of weak axial and vector coupling constants.

For first-forbidden (FF) transitions, the shape factor is

$$C(W) = k + kaW + kb/W + kcW^2, \tag{5}$$

where the coefficients $k, ka, kb,$ and kc depend on the FF nuclear matrix elements, the maximum electron energy, W_0, and the quantity $\xi = \alpha Z/(2R)$ with R the radius of a uniformly charged sphere approximating the nuclear charge distribution [34]. Following the treatment of Behrens and Bühring [35] they are given by

$$\begin{aligned}
k &= \left[\zeta_0^2 + \tfrac{1}{9}w^2\right]^{(0)} + \left[\zeta_1^2 + \tfrac{1}{9}(x+u)^2 - \tfrac{4}{9}\mu_1\gamma_1 u(x+u)\right.\\
&\quad \left. + \tfrac{1}{18}W_0^2(2x+u)^2 - \tfrac{1}{18}\lambda_2(2x-u)^2\right]^{(1)}\\
&\quad + \left[\tfrac{1}{12}z^2(W_0^2-\lambda_2)\right]^{(2)},\\
ka &= \left[-\tfrac{4}{3}uY - \tfrac{1}{9}W_0(4x^2+5u^2)\right]^{(1)} - \left[\tfrac{1}{6}z^2W_0\right]^{(2)},\\
kb &= \tfrac{2}{3}\mu_1\gamma_1\{-[\zeta_0 w]^{(0)} + [\zeta_1(x+u)]^{(1)}\},\\
kc &= \tfrac{1}{18}[8u^2 + (2x+u)^2 + \lambda_2(2x-u)^2]^{(1)}\\
&\quad + \tfrac{1}{12}[z^2(1+\lambda_2)]^{(2)}
\end{aligned} \tag{6}$$

with

$$\begin{aligned}
V &= \xi' v + \xi w', \quad \zeta_0 = V + \tfrac{1}{3}wW_0,\\
Y &= \xi' y - \xi(u'+x'), \quad \zeta_1 = Y + \tfrac{1}{3}(u-x)W_0.
\end{aligned} \tag{7}$$

The numbers in parentheses after the closing brackets denote the rank of the operators inside the brackets. The parameter γ_1 is given by $\sqrt{1-(\alpha Z)^2}$. For the Coulomb functions μ_1 and λ_2 we use the approximations $\mu_1 \approx 1$ and $\lambda_2 \approx 1$ [36].

After a nonrelativistic reduction, the matrix elements can be related to the form-factor coefficients, ${}^{A,V}F_{Kls}$, defined in Refs. [35,36]. In the Condon and Shortley phase convention [37] the matrix elements are

$$w = -R\,{}^A F^0_{011} = -g_A\sqrt{3}\frac{\langle f|\left|\sum_k r_k\left[\boldsymbol{C}_1^k \times \boldsymbol{\sigma}^k\right]^0 \boldsymbol{t}_-^k\right||i\rangle}{\sqrt{2J_i+1}}, \tag{8a}$$

$$x = -\frac{1}{\sqrt{3}}R\,{}^V F^0_{110} = -\frac{\langle f|\left|\sum_k r_k \boldsymbol{C}_1^k \boldsymbol{t}_-^k\right||i\rangle}{\sqrt{2J_i+1}}, \tag{8b}$$

$$u = -\sqrt{\frac{2}{3}}R\,{}^A F^0_{111} = -g_A\sqrt{2}\frac{\langle f|\left|\sum_k r_k\left[\boldsymbol{C}_1^k \times \boldsymbol{\sigma}^k\right]^1 \boldsymbol{t}_-^k\right||i\rangle}{\sqrt{2J_i+1}}, \tag{8c}$$

$$z = \frac{2}{\sqrt{3}}R\,{}^A F^0_{211} = 2g_A\frac{\langle f|\left|\sum_k r_k\left[\boldsymbol{C}_1^k \times \boldsymbol{\sigma}\right]^2 \boldsymbol{t}_-^k\right||i\rangle}{\sqrt{2J_i+1}}, \tag{8d}$$

$$w' = -\frac{2}{3} R\, {}^{A}F^{0}_{011}(1,1,1,1) = -g_A\sqrt{3}\frac{\langle f|\left|\sum_k \frac{2}{3} r_k I(1,1,1,1,r_k)\left[\boldsymbol{C}^k_1 \times \boldsymbol{\sigma}\right]^0 \boldsymbol{t}^k_-\right||i\rangle}{\sqrt{2J_i+1}}, \tag{8e}$$

$$x' = -\frac{2}{3\sqrt{3}} R\, {}^{V}F^{0}_{110}(1,1,1,1) = -\frac{\langle f|\left|\sum_k \frac{2}{3} r_k I(1,1,1,1,r_k)\boldsymbol{C}^k_1 \boldsymbol{t}^k_-\right||i\rangle}{\sqrt{2J_i+1}}, \tag{8f}$$

$$u' = -\frac{2\sqrt{2}}{3\sqrt{3}} R\, {}^{A}F^{0}_{111}(1,1,1,1) = -g_A\sqrt{2}\frac{\langle f|\left|\sum_k \frac{2}{3} r_k I(1,1,1,1,r_k)\left[\boldsymbol{C}^k_1 \times \boldsymbol{\sigma}^k\right]^1 \boldsymbol{t}^k_-\right||i\rangle}{\sqrt{2J_i+1}}, \tag{8g}$$

$$\xi' v = {}^{A}F^{0}_{000} = \frac{g_A\sqrt{3}}{M}\frac{\langle f|\left|\sum_k [\boldsymbol{\sigma}^k \times \boldsymbol{\nabla}^k]^0 \boldsymbol{t}^k_-\right||i\rangle}{\sqrt{2J_i+1}}, \tag{8h}$$

$$\xi' y = {}^{V}F^{0}_{101} = -\frac{1}{M}\frac{\langle f|\left|\sum_k \boldsymbol{\nabla}^k \boldsymbol{t}^k_-\right||i\rangle}{\sqrt{2J_i+1}}, \tag{8i}$$

where

$$\boldsymbol{C}_{lm} = \sqrt{\frac{4\pi}{2l+1}}\boldsymbol{Y}_{lm}, \tag{9}$$

with $\boldsymbol{Y}_{lm}$ the spherical harmonics. The weak axial coupling constant is $g_A = -1.2701(25)$ and M is the nucleon mass. The quantity $I(1,1,1,1,r)$ appearing in the primed matrix elements takes into account the nuclear charge distribution, which can be approximated by a uniform spherical distribution [35]:

$$I(1,1,1,1,r) = \frac{3}{2}\begin{cases}\left[1-\frac{1}{5}\left(\frac{r}{R}\right)^2\right] & 0 \leqslant r \leqslant R,\\ \left[\frac{R}{r}-\frac{1}{5}\left(\frac{R}{r}\right)^3\right] & r \geqslant R.\end{cases} \tag{10}$$

Based on the conserved vector current theory and the assumption that the isospin is a good quantum number, the matrix element $\xi' y$ can be related to the x matrix element [38]:

$$\xi' y = E_\gamma x, \tag{11}$$

where energy E_γ is defined as the energy difference between the isobaric analog of initial state and the final state:

$$E_\gamma = E_{\mathrm{ias}(i)} - E_f = Q + \Delta E_C - (m_n c^2 - m_p c^2), \tag{12}$$

where m_n and m_p are the neutron and proton masses and ΔE_C is the Coulomb displacement energy between isobaric analog states that can be approximated by [39]

$$\Delta E_C = 1.4136(1)\,\bar{Z}/A^{1/3} - 0.91338(11)\ \mathrm{MeV}, \tag{13}$$

with $\bar{Z} = (Z_i + Z_f)/2$.

To compare the first-forbidden and Gamow-Teller transitions, we define the averaged shape factor as

$$\overline{C(W)} = f/f_0, \tag{14}$$

where f takes the form of Eq. (2) and f_0 is

$$f_0 = \int_1^{W_0} F(Z,W)(W^2-1)^{1/2} W (W_0 - W)^2 dW. \tag{15}$$

III. MODEL SPACES AND QUENCHING

We have performed β-decay half-life calculations for r-process waiting points based on large-scale shell-model calculations. In particular, we chose the following model spaces and respective interactions.

For the $N = 50$ nuclei, we have adopted a model space spanned by the $0f_{7/2,5/2}$ and $1p_{3/2,1/2}$ orbits for protons and by the $0f_{5/2}$, $1p_{3/2,1/2}$, and $0g_{9/2}$ orbits for neutrons. The single-particle energies and the residual interaction are the ones adopted in Ref. [40] to study the shell evolution between ^{68}Ni and ^{78}Ni.

Our shell model calculations for the $N = 82$ waiting-point nuclei follows the shell-model studies presented in Ref. [19]. From the two model spaces defined in Ref. [19] we adopt the one built on a ^{88}Sr core. That is, we explicitly consider the $1p_{1/2}$ proton orbit, which is expected to be important for the description of the negative-parity states and hence the first-forbidden transitions. Our model space is then spanned by the $0g_{7/2}$, $1d_{3/2,5/2}$, $2s_{1/2}$, $0h_{11/2}$ orbits outside the $N = 50$ core for neutrons and the $1p_{1/2}$, $0g_{9/2,7/2}$, $1d_{3/2,5/2}$, $2s_{1/2}$ orbits for protons. This model space avoids spurious center-of-mass excitations by omitting the $0h_{11/2}$ orbit for protons and the $0g_{9/2}$ orbit for neutrons. We adopt the residual interaction given in Ref. [19] based on the ^{88}Sr core, which gives a good account of the spectroscopy of nuclei in the neighborhood of ^{132}Sn. In particular, our calculation reproduces the excitation energy of the first 1^+ state in ^{130}In as well as the low-energy spectrum of ^{128}Cd and of the r-process waiting-point nucleus ^{130}Cd [41].

The model space for the $N = 126$ waiting points has been spanned by the $0g_{7/2}$, $1d_{5/2,3/2}$, $0h_{11/2}$, and $2s_{1/2}$ orbits for protons and the $0h_{9/2}$, $1f_{7/2,5/2}$, $0i_{13/2}$, and $2p_{3/2,1/2}$ orbits for neutrons. As interaction, we use the effective Kuo-Herling interaction KHH$_e$ of Ref. [42], which has been constructed based on holes in a ^{208}Pb core. It is the same model space and effective interaction as has been used in a previous calculation of the half-lives, which, however, has only considered pure GT transitions [18]. These are mainly connected to neutron $0h_{9/2}$ to proton $0h_{11/2}$ transitions. However, it is expected that first-forbidden transitions can compete, mainly via neutron $0i_{13/2}$ to proton $0h_{11/2}$ transitions. Full diagonalization in this model space exceeds current computer capabilities. Hence, we performed truncated calculations following a generalize seniority scheme that allows for configurations with maximum seniority 8; that is, we consider a maximum of 4 non-$J = 0$ pairs, for even-even nuclei. For odd-even nuclei, the number of broken pairs had to be limited to three, while for ^{199}Ta no limitation has been enforced. We expect our model spaces to be large enough to give a reasonable account for the low-lying Gamow-Teller and first-forbidden transitions. Nevertheless, the model spaces are too restricted to recover the full Gamow-Teller and first-forbidden strengths built on the ground or isomeric states. The missed strength, however, resides mainly outside the Q_β window and hence does not affect our half-life calculations.

Although the shell model usually gives a good account of the relative strength distributions, it overestimates the total strength. For Gamow-Teller transitions, this shortcoming can

be corrected by replacing the bare Gamow-Teller operator with an effective operator $\mathrm{GT}_{\mathrm{eff}} = q\ \boldsymbol{\sigma t}$. The quenching factor q has been found to be approximately constant over the nuclear chart [43–45]. In practice, using $q \approx 0.7$ has been shown to give a good reproduction of the absolute Gamow-Teller distributions. There is also evidence that the absolute first-forbidden transition strength is overestimated within shell-model approaches. Ejiri and collaborators [46,47] related this fact to core polarization effects and suggested the introduction of a constant hindrance factor. Based on perturbation theory, Warburton [42,48] showed that the quenching of first-forbidden transitions depends slightly on the initial and final single-particle orbits. In particular, Warburton found that transitions mediated by the rank 0 operator [Eq. (8h)] (called the relativistic matrix element) appear to be enhanced compared to the other first-forbidden transitions, due to meson exchange effects [49].

To treat the quenching of the Gamow-Teller and first-forbidden transitions in our shell-model calculations, we have assumed that the quenching factors are the same for all nuclei. Following the findings of Warburton [48,49], we have furthermore assumed that the quenching factors for the operators of rank 0, 1, and 2 contributing to the first-forbidden transitions as defined in Eq. (8) can be different. To determine these individual quenching factors, we have performed shell-model calculations for experimentally known β-decays of nuclei in the vicinity of the magic neutron numbers $N = 82$ and $N = 126$. Here, we have adopted a similar set of first-forbidden transitions of nuclei in the lead region as chosen in the study of Warburton [49], supplemented by the decays of the ground state of ^{205}Au ($N = 126$) and the $(1/2)^-$ isomeric states in ^{131}In ($N = 82$) and ^{129}In ($N = 80$), which are both known to decay by first-forbidden transitions. By performing a least-squares fit to the experimental data, we obtained the following quenching factors for the various matrix elements defined in Eq. (8):

$$\begin{aligned} q(\xi' v) &= 1.266, \quad q(w) = q(w') = 0.66, \\ q(x) &= q(x') = 0.51, \quad q(u) = q(u') = 0.38, \\ q(z) &= 0.42. \end{aligned} \tag{16}$$

The calculated half-lives and the corresponding average shape factors are summarized in Table I. Figure 1 compares the experimental and calculated shape factors.

Upon closer inspection, there is quite a good agreement between our shell-model half-lives for the isomeric states in the In isotopes and the experimental values. For the nuclei in the vicinity of $N = 126$, however, we find a noticeably larger scatter between calculation and data, but there are no systematic deviations. With the exception of the two ^{205}Au decays, where our calculation overestimates (to the $5/2^-$ state in ^{205}Hg) or underestimates (to the $1/2^-$ state) the average shape factor roughly by a factor of 9, we generally find agreement of our calculated $C(\bar{W})$ with data within a factor of 4. As already observed while determining the quenching factor for GT transitions in shell-model calculations [53], the description of a decay between specific states is noticeably more sensitive to nuclear structure effects than global quantities such as half-lives or total strengths. Hence we expect that our prescription of quenching for first-forbidden transitions yields a fair description of the $N = 126$ half-lives.

TABLE I. Comparison of calculated $\log f_0 t$ and $(\overline{C(W)})^{1/2}$ for first-forbidden transitions with experimental data [50–52].

Transition		$\log f_0 t$		$(\overline{C(W)})^{1/2}$	
Initial	Final	Theory	Expt.	Theory	Expt.
^{131}In($\frac{1}{2}^-$)	^{131}Sn($\frac{3}{2}^+$)	5.32	≈5.1	65.8	85.4
	^{131}Sn($\frac{1}{2}^+$)	5.74	6.5	41.1	17.1
^{129}In($\frac{1}{2}^-$)	^{129}Sn($\frac{3}{2}^+$)	5.57	5.9(3)	49.8	34(12)
	^{129}Sn($\frac{1}{2}^+$)	5.80	5.5(1)	38.1	54(6)
^{205}Hg($\frac{1}{2}^-$)	^{205}Tl($\frac{1}{2}^+_1$)	5.37	5.257(11)	62.3	71.3(9)
	^{205}Tl($\frac{1}{2}^+_2$)	6.77	7.03(25)	12.5	9(3)
	^{205}Tl($\frac{3}{2}^+_1$)	7.26	6.51(21)	18.9	17(4)
	^{205}Tl($\frac{3}{2}^+_2$)	6.32	7.61(22)	10.3	5(1)
	^{205}Tl($\frac{5}{2}^+$)	8.16	8.70(21)	1.91	1.3(3)
^{206}Hg(0^+)	^{206}Tl(0^-)	5.42	5.41(6)	59.2	60(4)
	^{206}Tl(1^-_1)	5.18	5.24(10)	77.6	73(8)
	^{206}Tl(1^-_2)	5.68	5.67	43.6	44.3
^{207}Tl($\frac{1}{2}^+$)	^{207}Pb($\frac{1}{2}^-$)	5.14	5.108(6)	81.7	84.5(6)
	^{207}Pb($\frac{3}{2}^-$)	6.18	6.157(22)	24.7	25.3(6)
^{206}Tl(0^-)	^{206}Pb(0^+_1)	5.42	5.1775(13)	52.4	78.0(1)
	^{206}Pb(0^+_2)	5.18	5.99(6)	32.4	31(2)
	^{206}Pb(2^+)	5.68	8.60(3)	1.87	1.52(5)
^{205}Au($\frac{3}{2}^+$)	^{205}Hg($\frac{1}{2}^-_1$)	6.79	5.79(9)	12.1	39(4)
	^{205}Hg($\frac{3}{2}^-_1$)	7.33	6.43(11)	6.5	18(2)
	^{205}Hg($\frac{5}{2}^-_1$)	5.82	6.37(12)	37.3	20(3)

As was stressed by Warburton [49], the relativistic matrix element [Eq. (8h)] is enhanced compared to the other first-forbidden transitions. We confirm this finding as the value for $q(\xi' v)$ is noticeably larger than the other quenching factors.

Having determined the quenching of first-forbidden transitions, we adjust the quenching of the Gamow-Teller transition to the half-life of ^{130}Cd, which is expected to decay predominantly by Gamow-Teller. This is indeed borne out in our calculation. Using the quenching factor $q_{\mathrm{GT}} = 0.66$, we reproduce the measured half-life using both GT and first-forbidden transitions. The latter contribute about 13% to

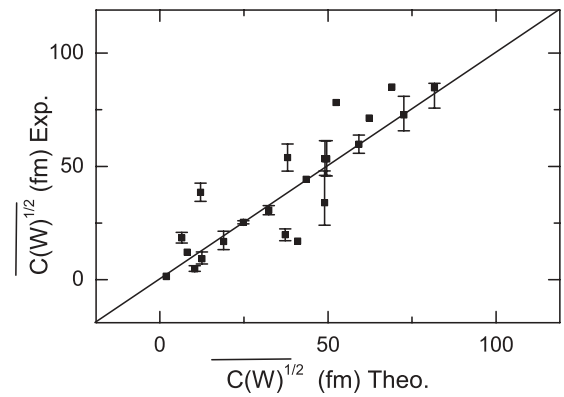

FIG. 1. Comparison of calculated first-forbidden average shape factors, obtained for the best-fit values of the quenching factors [Eq. (16)], with experimental data [50–52].

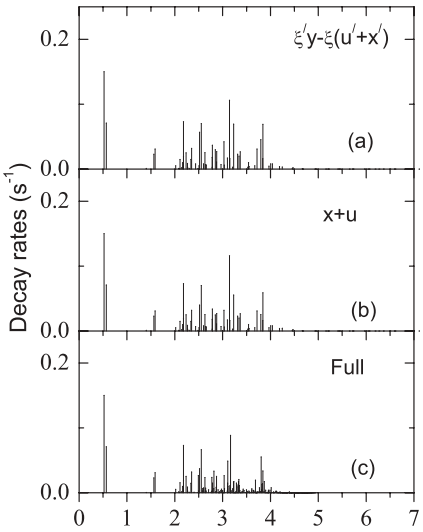

FIG. 2. Partial decay rates for ^{199}Ta calculated from first-forbidden rank 1 transitions only. Panels (a) and (b) show the decay rates obtained by using the linear combinations $\xi' y - \xi(x+u)$ and $(x+u)$, respectively, as pivot elements to calculate the contributions of rank 1 operators within a Lanczos scheme with 100 iterations. Panel (c) shows the partial decay rate using a Lanczos scheme with 300 iterations in which the states within the Q_β window are converged. These shell-model calculations have been performed in a truncated model space compared to other studies of the $N = 126$ isotones.

the half-life and hence are small but not negligible. Our factor $q_{\rm GT}$ is only slightly smaller than the customary quenching value of 0.7.

All half-lives presented in the next sections for the r-process waiting-point nuclei have been obtained using the quenching factors for Gamow-Teller and first-forbidden transitions derived above.

Before we present our results, we have to discuss another potential shortcoming of our calculations of first-forbidden transitions and how we handle it. A completely converged calculation of the first-forbidden transition strength in our chosen model space is prohibited due to computational limitations. We have derived the strength within the Lanczos scheme using 100 iterations. As a consequence, the lowest states are converged and correspond to physical states, while the Lanczos states at higher excitation energies are unphysical and represent strength per energy interval. Furthermore, their energy positions depend on the sum rule (pivot) state used for the calculation of the strength function. For example, starting from the pivot state of the x operator, one obtains different energy positions for the nonconverged states than when starting from the sum rule state of the u operator. As we need to compute superpositions of operators like $u + x$, where both the magnitude and the phase of the individual operators matter, we have followed the same procedure as used in shell-model calculations of double-β decays [31]. Hence, we start with an arbitrary sum rule state that can be any linear combination of operators of the same rank. During the Lanczos iteration procedure, we compute the overlaps with the individual operators. This iteration procedure is stopped when at least 80% of the total strength for each individual operator is recovered.

To illustrate this point, we have performed calculations for ^{199}Ta in the model space defined above and have used two different linear combinations of rank 1 operators, $\xi' y - \xi(x + u)$ and $(x + u)$, as pivots for the Lanczos calculations of the operators x and u. For the combination $\xi' y - \xi(x + u)$ we

TABLE II. Comparison of the present shell model half-lives and the ones of Ref. [18]. All half-lives are in seconds.

Nucleus	Half-life (s)		
	Expt.	Present	Shell model (Ref. [18])
^{82}Ge	4.55 ± 0.05	6.90	2.057
^{81}Ga	1.217 ± 0.005	1.03	0.577
^{80}Zn	0.545 ± 0.016	0.53	0.432
^{79}Cu	0.188 ± 0.025	0.27	0.222
^{78}Ni	$0.11^{+0.1}_{-0.06}$	0.15	0.127
^{77}Co		0.016	0.016
^{76}Fe		8.26×10^{-3}	7.82×10^{-3}
^{75}Mn		3.66×10^{-3}	3.52×10^{-3}
^{74}Cr		2.23×10^{-3}	2.07×10^{-3}

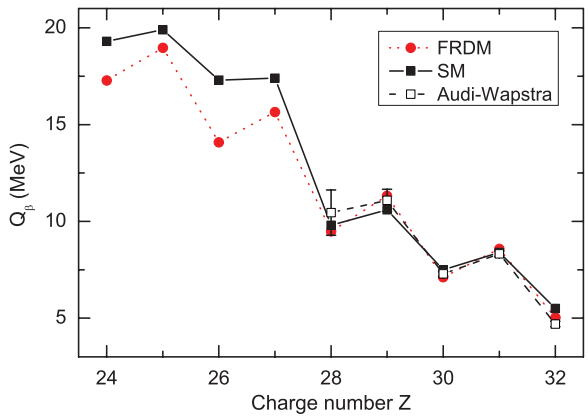

FIG. 3. (Color online) Comparison of Q_β values of the $N = 50$ isotones between experimental data [54] and theoretical results from FRDM [14] and the present shell-model approach.

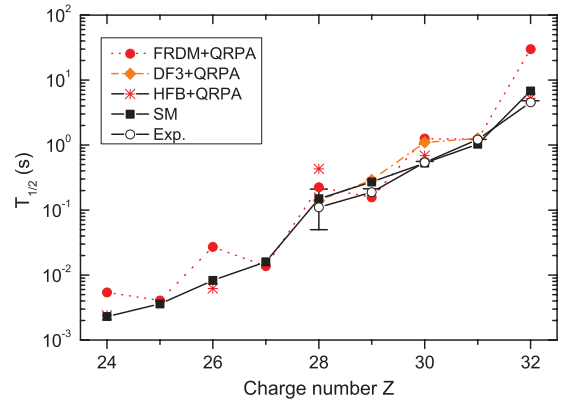

FIG. 4. (Color online) Comparison of half-lives of the $N = 50$ isotones between experimental data and theoretical results from FRDM + QRPA [14], HFB + QRPA [16], DF3 + QRPA [20,55], and the present shell-model approach.

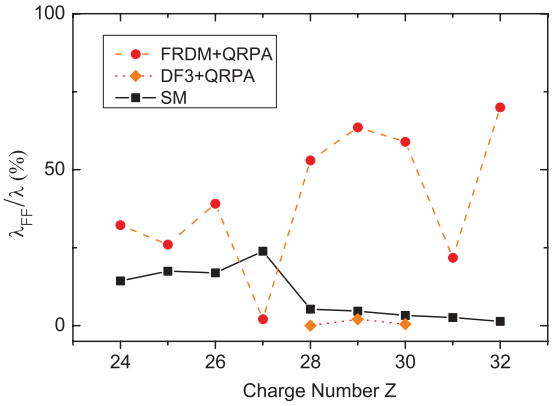

FIG. 5. (Color online) Percentage of the contributions from first-forbidden transitions to the half-lives of the $N = 50$ isotones from FRDM + QRPA [14], DF3 + QRPA [20,55], and the present shell model.

obtain 92% and 80% of the total strength for the operators x and u, respectively, while for the combination $x + u$ we recover 85% and 95% after 100 iterations. We stress that these shortcomings have a small effect on the first-forbidden half-lives that are dominated by the contribution of low-lying states, which converge in our Lanczos scheme and are strongly enhanced by the phase space energy dependence.

To quantify the potential uncertainty in our first-forbidden half-lives, we have performed calculations for ^{199}Ta in the model space as defined above but allowing only one proton pair to be broken in our seniority scheme. This truncated space allows for the calculation of a fully converged first-forbidden strength distribution in the Q_β window. Figure 2 compares the partial decay rates to the various states in the daughter nucleus obtained in the fully converged calculation (with 300 Lanczos iterations) with those where the rank 1 contributions were derived using the linear combinations $\xi' y - \xi(x + u)$ and $(x + u)$ as pivots for the Lanczos scheme with 100 iterations. As expected, the lowest Lanczos states are converged and hence the calculated strength is the same for either choice of pivot combination. The Lanczos scheme with 100 iterations is not sufficient to converge the states for excitation energies larger than about 2.5 MeV. They represent unphysical states as discussed above. Obviously, further iterations lead to a stronger fragmentation of the strength in a small energy interval around the unphysical states. The energy interval is small enough that this redistribution of strength due to different phase-space weighting has negligible effect on the half-life. However, the interference contributions also lead to rather mild differences between the truncated and the converged calculations. We find a partial half-life due to rank 1 first-forbidden operators of 655 and 716 ms when calculating the rank 1 operators from the linear combinations $\xi' y - \xi(x + u)$ and $(x + u)$, respectively, while the partial half-life in the converged study is 651 ms, in agreement within 10% of the two approximate calculations. In the following, we calculate the contributions from the first-forbidden rank 1 operators using a Lanczos scheme with the pivot state $\xi' y - \xi(x + u)$ and 100 iterations.

IV. HALF-LIVES OF THE $N = 50$ WAITING-POINT NUCLEI

To calculate half-lives, a good description of the transition matrix elements and also of the Q_β values is required. As is demonstrated in Fig. 3, our shell-model calculation reproduces the Q_β values as given in the Audi-Wapstra compilation well

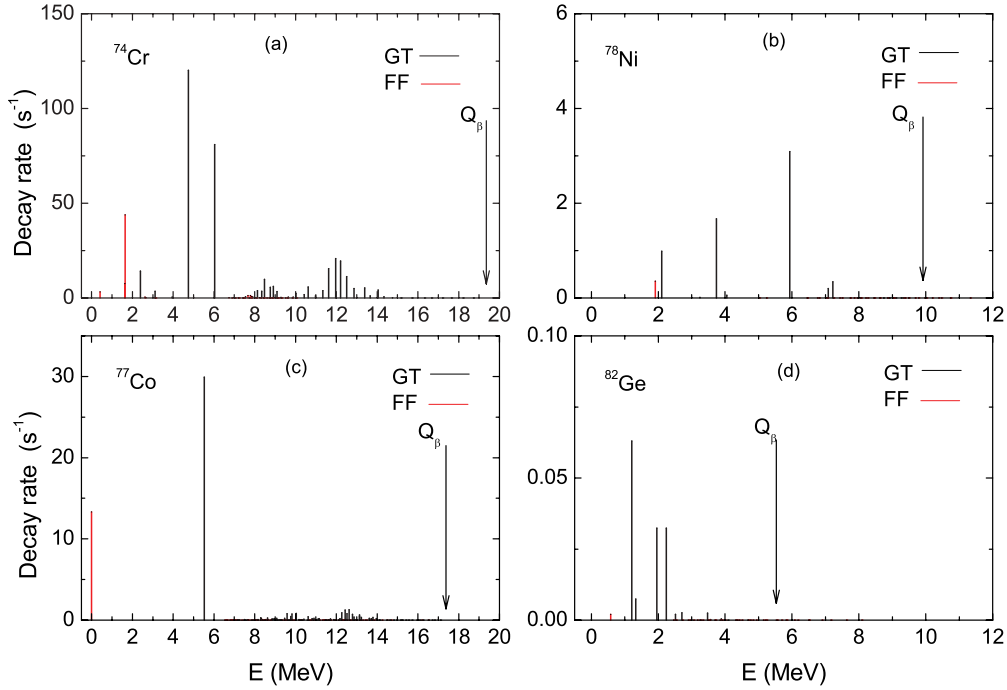

FIG. 6. (Color online) Partial decay rates including GT and FF transitions for the $N = 50$ isotones ^{74}Cr (a), ^{78}Ni (b), ^{77}Co (c), and ^{82}Ge (d).

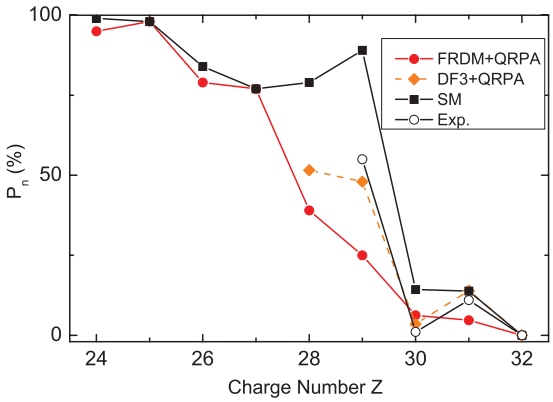

FIG. 7. (Color online) Neutron emission probability for $N = 50$ isotones from FRDM + QRPA [14], DF3 + QRPA [20,55], the present shell model, and the experiment [52].

[54]. Hence, we use the shell-model Q_β values in the following calculation of the half-lives and β-delayed neutron emission probabilities for the $N = 50$ waiting-point nuclei.

As shown in Table II and Fig. 4, the shell-model half-lives agree quite well with the data, although they overestimate the ones of ^{82}Ge and ^{79}Cu by about 50%. Nevertheless, the agreement is significantly better than that obtained based on the global FRDM and ETFSI models. The HFB results [16], which are restricted to the decay of even-even nuclei, are very similar to the shell-model results, except for the half-life of the double-magic nucleus ^{78}Ni. Here, only the shell-model reproduces the measured value [7], while all other models predict a significantly longer half-life. This underlines the fact that many-body configuration mixing is needed to reproduce the cross-gap correlations in double-magic nuclei. Similar results have been found in studies of the isotope shifts in calcium [56] and the M1 strength distributions in argon isotopes [57].

The contribution of first-forbidden transitions to the $N = 50$ half-lives is shown in Fig. 5. For the decay of the nuclei with $Z \geqslant 28$ the probability is very small (less than 5%). However, first-forbidden transitions contribute about 25% to the ^{77}Co

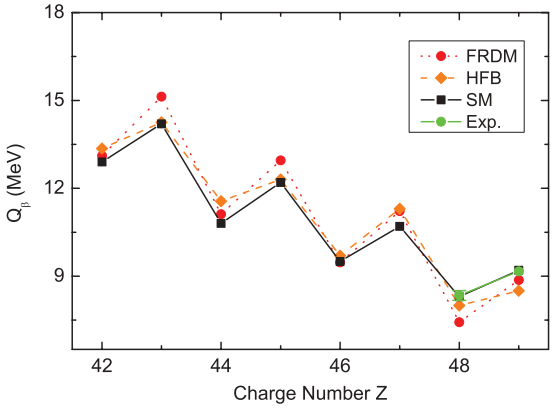

FIG. 8. (Color online) Comparison of Q_β values of the $N = 82$ isotones between theoretical results from the FRDM [14], HFB [16], the present shell-model approaches, and experimental data [52].

TABLE III. Comparison of the present shell-model half-lives and the ones of Ref. [19] with experimental data [50,58]. All half-lives are in milliseconds.

Nucleus	Half-life (ms)		
	Expt.	Present	Shell model (Ref. [19])
^{131}In	280 ± 30	247.53	260
^{130}Cd	162 ± 7	164.29	162
^{129}Ag	46^{+5}_{-9}	69.81	70
^{128}Pd		47.25	46
^{127}Rh		27.98	27.65
^{126}Ru		20.33	19.76
^{125}Tc		9.52	9.44
^{124}Mo		6.21	6.13

decay, while they are smaller but still sizable for the decay of the nuclei with charge numbers $Z = 24$–26.

To understand this behavior, we note that first-forbidden contributions are related to the transition from a $g_{9/2}$ neutron orbital to a $f_{7/2}$ proton orbital for the rank 1 operators and to a $f_{5/2}$ proton orbital for rank 2 operators. (There are no contributions from rank 0 operators in our model space.) In the simple independent particle model, the $f_{7/2}$ level gets completely occupied for ^{78}Ni and consequently this transition is Pauli-blocked for $N = 50$ nuclei with $Z \geqslant 28$. In the shell model, the blocking is partially removed by configuration mixing, but the importance of the first-forbidden transitions stays low. For these nuclei, they are nearly exclusively due to contributions from the rank 2 operators. For the nuclei with $Z < 28$, the proton $f_{7/2}$ orbital is not fully occupied and first-forbidden transitions due to the rank 1 operators are possible. They are noticeably larger those of the rank 2 operators. Hence, the total first-forbidden strength is significantly larger for nuclei with $Z < 28$ than for the nuclei with $Z \geqslant 28$. Furthermore, it increases with decreasing charge number due to the depopulation of the proton $f_{7/2}$ orbital in the daughter nucleus. However, Gamow-Teller transitions from the neutron $f_{5/2}$ orbital into the proton $f_{7/2}$ orbital become unblocked. Hence, reducing the charge number increases both the GT and first-forbidden transitions due to decreasing Pauli blocking of

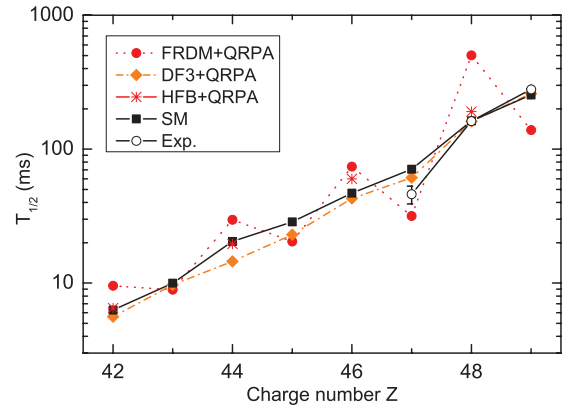

FIG. 9. (Color online) Comparison of half-lives of the $N = 82$ isotones as calculated in the FRDM, HFB, DF3 + QRPA [20], and the present shell-model approaches with data.

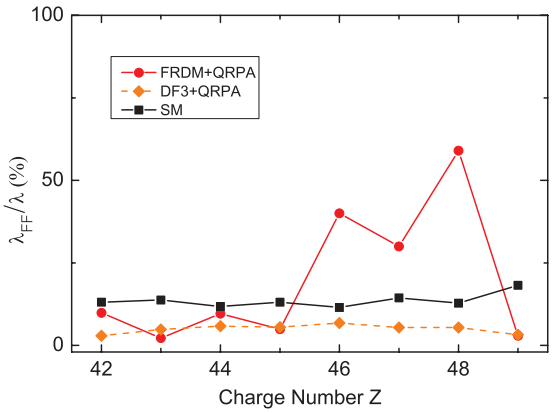

FIG. 10. (Color online) Percentage of the contributions from first-forbidden transitions to the half-lives of the $N = 82$ isotones from FRDM + QRPA [14], DF3 + QRPA [20,55], and the present shell-model data.

the dominant transitions into the $f_{7/2}$ orbital. However, the relative decrease for the GT half-lives with decreasing charge number is stronger than for the first-forbidden transitions. This is related to phase space. Examples of differential decay rates as function of excitation energies for nuclei ^{74}Cr, ^{77}Co, ^{78}Ni, and ^{82}Ge are shown in Fig. 6. From these figures we note that the first-forbidden transitions dominantly proceed to daughter states at low excitation energies (usually up to 2–2.5 MeV) for the $N = 50$ nuclei with $Z < 28$, while the GT transitions go to states with excitation energies on the order of 5–7 MeV, simply reflecting the fact that it is energetically more favorable to have a $f_{5/2}$ neutron hole and a closed $g_{9/2}$ shell than to have a hole in the $g_{9/2}$ orbital. As the energy gain in the transitions is smaller for the GT transitions, they are more sensitive to the increase of the Q_β value with decreasing charge number. This explains why the relative contribution of first-forbidden transitions decreases with reduced charge number below the double-magic ^{78}Ni. Above ^{78}Ni, the GT transitions proceed to daughter states at relatively low excitation energies. (Figure 6 shows the differential decay rates for ^{82}Ge as an example.) As a consequence, first-forbidden transitions, due to their smaller transition matrix elements, cannot compete with GT transitions.

We have used the shell-model neutron separation energies to calculate the β-delayed neutron emission probabilities, which are shown in Fig. 7. As demonstrated above, GT transitions dominate the decays of the $N = 50$ r-process waiting points. As for the nuclei with $Z \leqslant 29$, these transitions connect mainly to daughter states at excitation energies above the respective neutron threshold, and the decay is accompanied by a high degree of neutron emission. The probability comes close to 100% for the decays of ^{55}Mn and ^{54}Cr associated with the very low neutron separation energies in the daughters. For the nuclei with $Z > 29$, the GT transitions reside at lower excitation energies in the respective daughters, while the neutron thresholds increases. As a result, the neutron emission probability is strongly reduced in these nuclei.

V. HALF-LIVES OF THE $N = 82$ WAITING-POINT NUCLEI

The present interaction and model spaces, based on a ^{88}Sr core, are not the same as used in Ref. [19] to calculate Q_β values and Gamow-Teller strength functions. However, we stress that the present shell-model calculation gives results very similar to the ones of Ref. [19]. In particular, we reproduce the experimentally available Q_β values very well, as shown in Fig. 8. This figure also shows that the agreement of the Q_β values obtained in other models is usually not as good as that by the shell-model results. In the following, we use the shell-model Q_β values for the calculation of the half-lives.

The $1/2^-$ isomer in ^{131}In corresponds approximately to a ^{132}Sn configuration with a hole in the $1p_{1/2}$ orbital. Our calculation reproduces the energy of the isomer at 0.302 MeV. (This quantity was one of the experimental ingredients to which the interaction has been adjusted.)

The calculated half-lives for the $N = 82$ waiting point nuclei are summarized in Table III and are compared to data and previous theoretical estimates in Fig. 9. Compared to experiment, the half-life of ^{131}In is well reproduced, while the one for ^{129}Ag is somewhat too long. This shortcoming had already been observed in the previous shell-model calculations. In

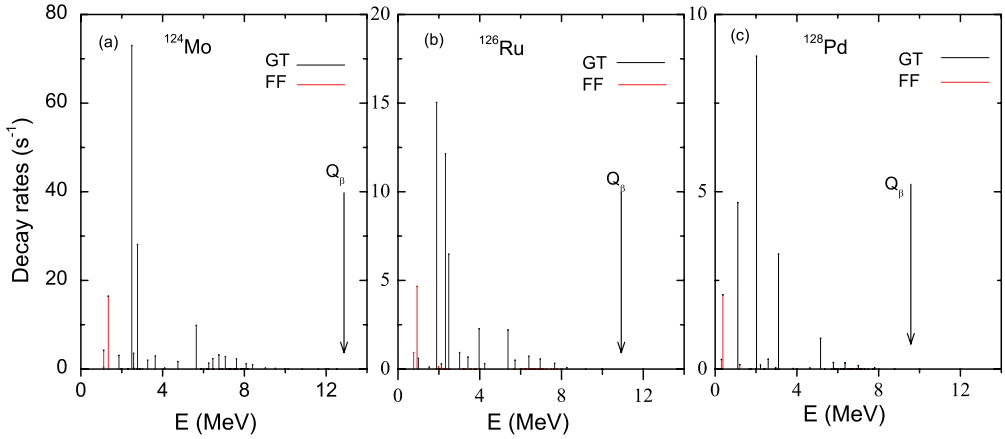

FIG. 11. (Color online) Partial decay rates including GT and FF transitions for the $N = 82$ isotones ^{124}Mo (a), ^{126}Ru (b), and ^{128}Pd (c).

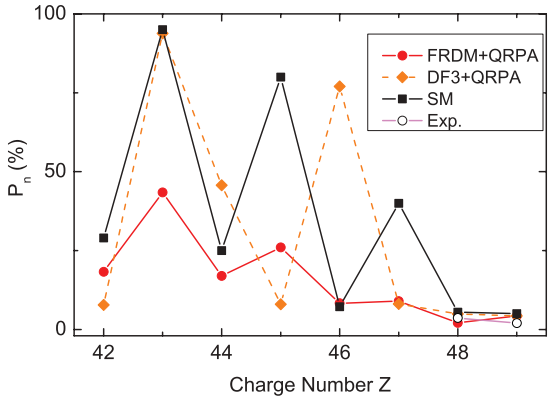

FIG. 12. (Color online) β-delayed neutron emission probability for selected $N = 82$ r-process nuclei from FRDM + QRPA [14], DF3 + QRPA [20,55], the present shell model, and experimental data [52].

fact, the present shell-model results, including contributions from first-forbidden transitions, agree very well with the shell-model results of Ref. [19]. However, this does not mean that first-forbidden transitions are negligible. As shown in Fig.10, first-forbidden transitions contribute about 13% to the half-life. However, this value is nearly the same for all $N = 82$ waiting-point nuclei, which explains the similarity between the present shell-model results and those of Ref. [19]. Only for ^{131}In do the first-forbidden transitions contribute somewhat more, resulting in a slightly smaller half-life than in the shell-model study based solely on Gamow-Teller transitions. We note that our prediction of an 18% contribution stemming from first-forbidden transitions to the decay of the ^{131}In ground state is in agreement with the experimental limit of $\leqslant$20%. We further add that we calculate a Gamow-Teller contribution to the half-life of the $1/2^-$ isomer in ^{131}In that is less than 1%, confirming our assumption to fix the quenching of the first-forbidden transition to this decay. Figure 11 shows the partial decay rates to different final states for the nuclei ^{124}Mo, ^{126}Ru, and ^{128}Pd. We note that Gamow-Teller transitions are larger than first-forbidden transitions, which proceed to levels at lower excitation energies and enhance them by phase space.

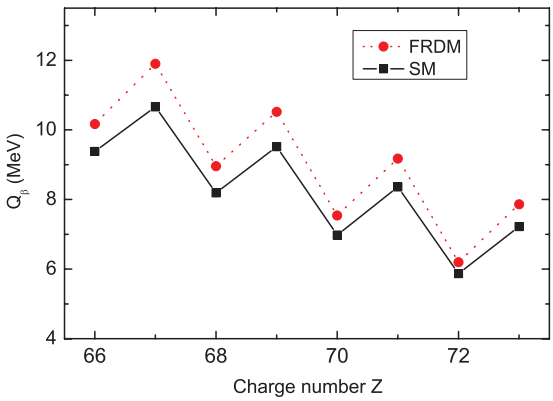

FIG. 13. (Color online) Comparison of Q_β values of the $N = 126$ isotones as calculated in the FRDM [14] and the present shell-model approaches.

TABLE IV. Comparison of the present shell-model half-lives and the ones of Ref. [59]. All half-lives are in milliseconds.

Nucleus	Half-life (ms)	
	Present	Shell model (Ref. [59])
^{199}Ta	286.17	278.88
^{198}Hf	193.28	129.65
^{197}Lu	107.85	84.81
^{196}Yb	68.98	44.18
^{195}Tm	36.03	29.49
^{194}Er	24.58	18.11
^{193}Ho	13.58	10.94
^{192}Dy	10.10	7.75

The β-delayed neutron emission probabilities (i.e., the probabilities that the decay leads to states in the daughter nucleus above the neutron separation threshold and hence is followed by the emission of a neutron) is obviously sensitive to a good description of both the neutron separation energies and the β strength functions in the Q_β window. As has been stressed in Refs. [17,19], the improved description of correlations in shell-model calculations gives a more realistic account of the fragmentation of the strength function than is obtained in QRPA studies. Figure 12 compares the present shell-model probabilities to those obtained in Ref. [19]. We find that the inclusion of first-forbidden transitions leads only to minor changes. A detailed comparison of the shell-model results [19] to those obtained in other theoretical approaches is given in Refs. [17,19].

VI. HALF-LIVES OF THE $N = 126$ WAITING-POINT NUCLEI

Figure 13 compares the calculated Q_β values of the $N = 126$ isotones with other theoretical models. While the general trend of Q_β is quite similar to that obtained in the FRDM model, the shell-model values are slightly smaller than those from the FRDM model. However, as no experimental data exist for these very neutron-rich $N = 126$ nuclei, it is not possible

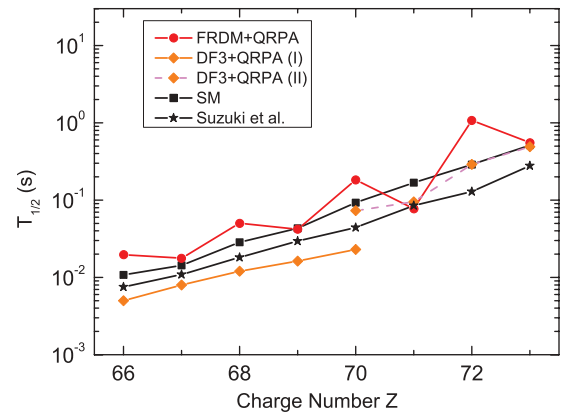

FIG. 14. (Color online) Comparison of half-lives of the $N = 126$ isotones as calculated in the FRDM + QRPA, DF3 + QRPA(I) [20], DF3 + QRPA(II) [60], and the present shell model approaches [59].

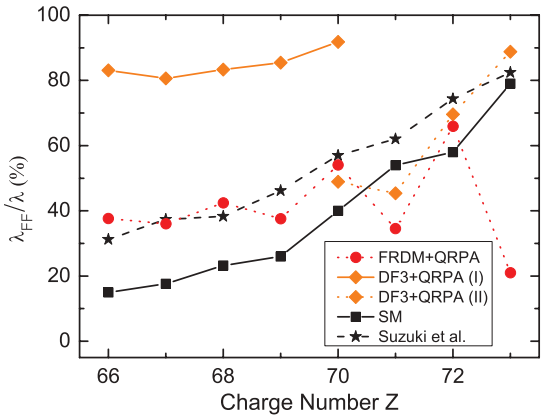

FIG. 15. (Color online) Percentage of the contributions from first-forbidden transitions to the half-lives of the $N = 126$ isotones are compared with results from DF3 + QRPA(I) [20], DF3 + QRPA(II) [60], and shell-model approaches [59].

to decide which Q_β are more realistic. In the following, we use the shell-model values to calculate the half-lives and β-delayed neutron emission probabilities for the $N = 126$ r-process waiting-point nuclei.

The shell model half-lives are listed in Table IV and are compared to other theoretical predictions in Fig. 14. Although recently researchers at GSI have successfully measured the half-lives of nuclei close to $N = 126$ with charge numbers below lead [12], supplying important constraints about the half-life trend toward the r-process nuclei, experimental data for the $N = 126$ r-process nuclei do yet not exist. Hence, our results can be compared only to other theoretical predictions. We note that the present half-lives for $Z > 70$ are faster, by about a factor of two, than those obtained by Borzov within a QRPA approach on top of the density functional DF3, showing a similar dependence on charge number [55]. Adopting a different parametrization, Borzov has also calculated half-lives for $N = 126$ isotones with $Z < 70$, which are slightly faster than the shell-model values [61]. The shell model half-lives are noticeably faster than those predicted previously by global models, for example, by the QRPA calculation on top of the microscopic-macroscopic FRDM or ETFSI approaches.

Recently Suzuki *et al.* [59] have presented the first shell-model half-lives for $N = 126$ r-process nuclei, including both GT and first-forbidden contributions. However, our present model space including the ($0g_{7/2}$, $1d_{5/2,3/2}$, $0h_{11/2}$, $2s_{1/2}$) proton orbits is noticeably larger than the one used in Ref. [59] (the $1d_{3/2}$, $0h_{11/2}$, $2s_{1/2}$ proton orbits). The two shell-model calculations differ in the residual interaction and additionally in the adopted quenching scheme for first-forbidden transitions. Nevertheless, as is shown in Table IV and Fig. 14, both shell model calculations predict very similar half-lives for the $N = 126$ nuclei. Both studies do not predict the strong odd-even staggering in the half-lives as observed in the QRPA results on top of the FRDM model.

As already noted in Ref. [20], based on the density functional calculations, first-forbidden transitions are expected to contribute significantly to the half-lives of the $N = 126$ r-process nuclei. This finding is supported by our shell-model calculations (Fig. 15). One observes an increasing contribution from the first-forbidden transitions with increasing proton number. In fact, for nuclei with proton number $Z \geqslant 70$, contributions from first-forbidden transitions to the half-life dominate over Gamow-Teller transitions. This behavior can be understood by inspecting the partial decay rates arising from Gamow-Teller and first-forbidden transitions, which are shown in Fig. 16 for selected nuclei. We note that Gamow-Teller transitions are related to the change of a neutron in the $0h_{9/2}$ orbit to a proton in the $0h_{11/2}$ orbit, which, however, is fragmented over several states in the daughter nucleus due to correlations. Nevertheless, for the nuclei studied here, these final proton states reside at moderately high excitation energies around 3 MeV, while first-forbidden transitions connect to excited states at lower excitation energies. With increasing proton number, more protons occupy the final $0h_{11/2}$ orbit and the GT transitions get gradually Pauli blocked. This explains why the GT strength gets strongly reduced with increasing

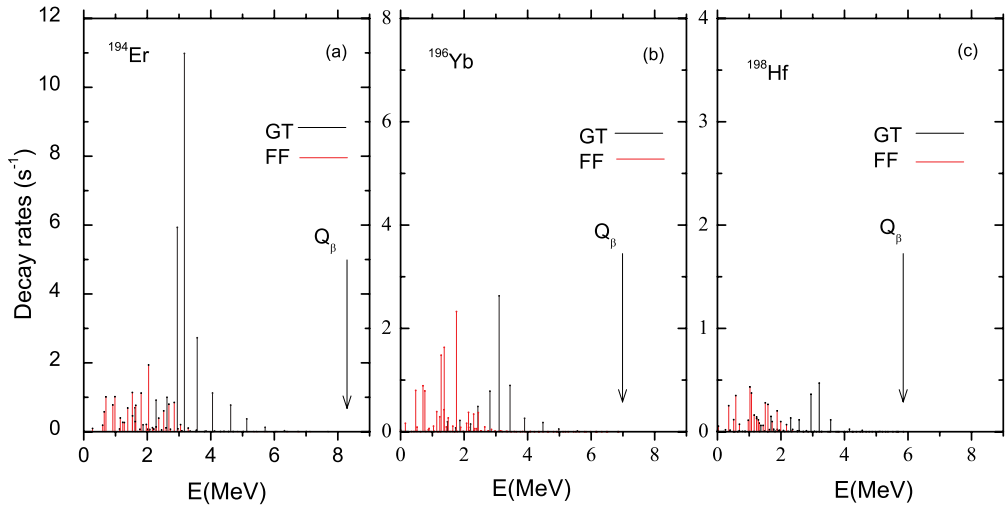

FIG. 16. (Color online) Partial decay rates including Gamow-Teller and FF transitions for the $N = 126$ isotones ^{194}Er (a), ^{196}Yb (b), and ^{198}Hf (c).

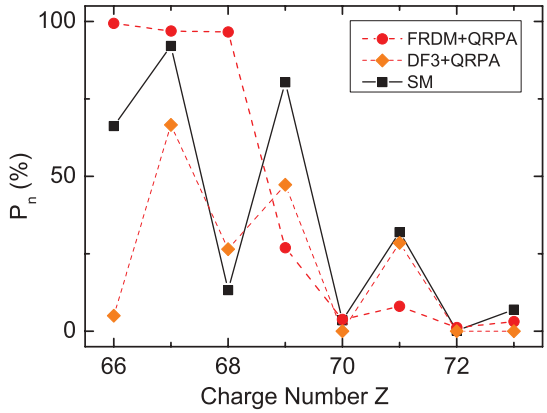

FIG. 17. (Color online) Neutron emission probability of $N = 126$.

proton number. Actually, first-forbidden transitions also get blocked with increasing proton number, which is a significantly milder effect than for the GT transitions. We note that for all nuclei studied here, first-forbidden transitions are mainly mediated by rank 0 and 1 operators (the latter contributes about 70% to the forbidden strength), while the contribution arising from rank 2 operators are very small. Due to its larger sensitivity to phase space ($\sim Q^7$) the relative contribution of rank 2 transitions increases slightly with decreasing charge number. For the $N = 126$ nuclei studied here, the depopulation of the $0h_{11/2}$ proton orbital with decreasing charge number, which increases both the Gamow-Teller and first-forbidden transitions, dominates the trend observed in our half-lives. Changes in phase space and pairing have lesser effects on our half-life systematics.

Gamow-Teller transitions proceed to final states mainly above the neutron threshold and hence are accompanied by neutron emission, while the final states populated by first-forbidden transition predominantly reside below the neutron threshold. Hence, we expect from the Z dependence of the GT and first-forbidden transitions that the β-delayed neutron emission probability decreases with increasing proton number. This is indeed confirmed by Fig. 17. The striking odd-even staggering is related to pairing, which reduces the neutron threshold energies in odd-odd daughter nuclei relatively to odd-A nuclei but basically does not affect the strength distributions, as discussed in Ref. [62]. The QRPA-FRDM neutron emission probabilities show a rather abrupt increase at $Z = 68$, which is likely due to the fact that QRPA calculations show significantly less fragmentation of the strength than shell-model studies and that, for $Z < 69$, the few dominant transitions reside above the neutron threshold.

VII. SUMMARY AND CONCLUSIONS

We have calculated the half-lives and β-delayed neutron emission probabilities of the r-process waiting-point nuclei with magic neutron numbers $N = 50$, 82, and 126 within the framework of the large-scale shell model. The calculations include contributions both from allowed Gamow-Teller and first-forbidden transitions. We find good agreement with the existing experimental data, i.e., the half-lives for the $N = 50$ nuclei with charge numbers $Z = 28$–32 and for the $N = 82$ nuclei ^{129}Ag and ^{130}Cd. In our calculations, first-forbidden transitions significantly reduce the half-lives of the $N = 126$ waiting-point nuclei, while they have a smaller effect on the half-lives of the $N = 50$ and 82 r-process nuclei.

ACKNOWLEDGMENTS

This work was supported by the Helmholtz International Center for FAIR within the framework of the LOEWE program launched by the state of Hesse, the Helmholtz Association through the Nuclear Astrophysics Virtual Institute (VH-VI-417), the ExtreMe Matter Institute (EMMI) in the framework of the Helmholtz Alliance HA216/EMMI, the Deutsche Forschungsgemeinschaft through Contract No. SFB 634, the National Natural Science Foundation of China (11165006, 11105079), and the IN2P3-GSI collaboration agreement (10-63). Discussions with Frédéric Nowacki are gratefully acknowledged.

[1] E. M. Burbidge, G. R. Burbidge, W. A. Fowler, and F. Hoyle, Rev. Mod. Phys. **29**, 547 (1957).
[2] A. G. W. Cameron, Pub. Astron. Soc. Pacific **69**, 201 (1957).
[3] J. J. Cowan, F.-K. Thielemann, and J. W. Truran, Phys. Rep. **208**, 267 (1991).
[4] K.-L. Kratz, J. P. Bitouzet, F.-K. Thielemann, P. Möller, and B. Pfeiffer, Ap. J. **403**, 216 (1993).
[5] S. E. Woosley, G. J. Mathews, J. R. Wilson, R. D. Hoffman, and B. S. Meyer, Astrophys. J. **433**, 229 (1994).
[6] K.-L. Kratz, F. K. Thielemann, W. Hillebrandt, P. Möller, V. Härms, A. Wöhr, and J. W. Truran, J. Phys. G **24**, S331 (1988).
[7] P. T. Hosmer *et al.*, Phys. Rev. Lett. **94**, 112501 (2005).
[8] K. L. Kratz *et al.*, in *Proccedings of the International Conference on Fission and Properties of Neutron-Rich Nuclei, Sanibel Island, 1997*, edited by J. H. Hamilton (World Scientific Press, Singapore, 1998).
[9] K.-L. Kratz, H. Gabelmann, W. Hillebrandt, B. Pfeiffer, K. Schlösser, and F.-K. Thielemann, Z. Phys. A **325**, 489 (1986).
[10] B. Pfeiffer, K.-L. Kratz, F.-K. Thielemann, and W. B. Walters, Nucl. Phys. A **693**, 282 (2001).
[11] S. Nishimura *et al.* Phys. Rev. Lett. **106**, 052502 (2011).
[12] T. Kurtukian-Nieto *et al.*, Nucl. Phys. A **827**, 587C (2009).
[13] P. Möller, J. R. Nix, and K.-L. Kratz, At. Data Nucl. Data Tables **66**, 131 (1997).
[14] P. Möller, B. Pfeiffer, and K.-L. Kratz, Phys. Rev. C **67**, 055802 (2003).
[15] I. N. Borzov, S. Goriely, and J. M. Pearson, Nucl. Phys. A **621**, 307C (1997).
[16] J. Engel, M. Bender, J. Dobaczewski, W. Nazarewicz, and R. Surman, Phys. Rev. C **60**, 014302 (1999).
[17] G. Martínez-Pinedo and K. Langanke, Phys. Rev. Lett. **83**, 4502 (1999).

[18] K. Langanke and G. Martínez-Pinedo, Rev. Mod. Phys. **75**, 818 (2003).
[19] J. J. Cuenca-García, G. Martínez-Pinedo, K. Langanke, F. Nowacki, and I. Borzov, Eur. Phys J. A **34**, 99 (2007).
[20] I. Borzov, Nucl. Phys. A **777**, 645 (2006).
[21] W. C. Haxton, arXiv:1209.3743 [nucl-th].
[22] E. Kolbe, K. Langanke, S. Krewald, and F.-K. Thielemann, Nucl. Phys. A **540**, 599 (1992).
[23] E. Kolbe, K. Langanke, G. Martínez-Pinedo, and P. Vogel, J. Phys. G: Nucl. Part. Phys. **29**, 2569 (2003).
[24] K. Langanke and E. Kolbe, At. Data. Nucl. Data Tables **79**, 293 (2001).
[25] K. Langanke and E. Kolbe, At. Data. Nucl. Data Tables **82**, 191 (2002).
[26] M. Terasawa, K. Langanke, T. Kajino, G. J. Mathews, and E. Kolbe, Astrophys. J. **608**, 470 (2004).
[27] S. E. Woosley, D. H. Hartmann, R. D. Hoffman, and W. C. Haxton, Astrophys. J. **356**, 272 (1990).
[28] A. Heger, E. Kolbe, W. Haxton, K. Langanke, G. Martínez-Pinedo, and S. E. Woosley, Phys. Lett. B **606**, 258 (2005).
[29] T. Yoshida *et al*., Astrophys. J. **686**, 448 (2008).
[30] T. Suzuki, A. B. Balantekin, and T. Kajino, Phys. Rev. C **86**, 015502 (2012).
[31] E. Caurier, G. G. Martinez-Pinedo, F. Nowacki, A. Poves, and A. P. Zuker, Rev. Mod. Phys. **77**, 427 (2005).
[32] E. Caurier and F. Nowacki, Acta Physica Polonica B **30**, 705 (1999).
[33] A. R. Edmonds, *Angular Momentum in Quantum Mechanics* (Princeton University Press, Princeton, NJ, 1960).
[34] W.-T. Chou, E. K. Warburton, and B. A. Brown, Phys. Rev. C **47**, 163 (1993).
[35] H. Behrens and W. Bühring, Nucl. Phys. A **162**, 111 (1971).
[36] H. Behrens and W. Bühring, *Electron Radial Wave Functions and Nuclear β-Decay* (Clarendon, Oxford, 1982).
[37] K. Heyde, *The Nuclear Shell Model* (Springer-Verlag, Berlin, 1994).
[38] E. K. Warburton, J. A. Becker, B. A. Brown, and D. J. Millener, Ann. Phys. (NY) **187**, 471 (1988).
[39] M. S. Antony, A. Pape, and J. Britz, At. Data Nucl. Data Tables **66**, 1 (1997).
[40] K. Sieja and F. Nowacki, Phys. Rev. C **81**, 061303(R) (2010).
[41] A. Jungclaus *et al*., Phys. Rev. Lett. **99**, 132501 (2007).
[42] E. K. Warburton, Phys. Rev. C **44**, 233 (1991).
[43] B. H. Wildenthal, M. S. Curtin, and B. A. Brown, Phys. Rev. C **28**, 1343 (1983).
[44] K. Langanke, D. J. Dean, P. B. Radha, Y. Alhassid, and S. E. Koonin, Phys. Rev. C **52**, 718 (1995).
[45] G. Martínez-Pinedo, A. Poves, E. Caurier, and A. P. Zuker, Phys. Rev. C **53**, R2602 (1996).
[46] H. Ejiri, T. Shibata, and K. Satoh, Phys. Lett. B **38**, 73 (1972).
[47] H. Ejiri and J. J. Fujita, Phys. Rep. **38**, 85 (1978).
[48] E. K. Warburton, Phys. Rev. C **42**, 2479 (1990).
[49] E. K. Warburton and I. S. Towner, Phys. Rep. **242**, 103 (1994).
[50] B. Fogelberg *et al*., Phys. Rev. C **70**, 034312 (2004).
[51] L.-E. De Geer and G. B. Holm, Phys. Rev. C **22**, 2163 (1980).
[52] National Nuclear Data Center online retrieval system http://www.nndc.bnl.gov.
[53] E. Caurier, G. Martínez-Pinedo, A. Poves, and A. P. Zuker, Phys. Rev. C **52**, 1736 (1995).
[54] G. Audi *et al*., Nucl. Phys. A **729**, 337 (2003).
[55] I. N. Borzov and S. Goriely, Phys. Rev. C **62**, 035501 (2000).
[56] E. Caurier, K. Langanke, G. Martinez-Pinedo, F. Nowacki, and P. Vogel, Phys. Lett. B **522**, 240 (2001).
[57] A. F. Lisetskiy *et al*., Nucl. Phys. A **789**, 114 (2007).
[58] I. Dillmann *et al*., Phys. Rev. Lett. **91**, 162503 (2003).
[59] T. Suzuki, T. Yoshida, T. Kajino, and T. Otsuka, Phys. Rev. C **85**, 015802 (2012).
[60] I. Borzov, Phys. Atom. Nucl. **74**, 1435 (2011).
[61] T. Kurtukian *et al*., arXiv:0711.0101.
[62] K. Langanke and G. Martinez-Pinedo, Nucl. Phys. A **673**, 481 (2000).